

Proceedings of the ASME 2024 19th International Manufacturing Science and Engineering Conference MSEC2024

June 17-21, 2024, Knoxville, Tennessee

MSEC2024-124356

DIRECT MEASUREMENT OF TOOL-CHIP CONTACT STRESSES IN MACHINING USING FULL-FIELD PHOTOELASTICITY

Jobin T. Mathews*, Dinakar Sagapuram

Department of Industrial and Systems Engineering, Texas A&M University, College Station, TX 77843, USA

ABSTRACT

Tool-chip contact stresses are of major interest in developing a basic understanding of the mechanics of machining. The interfacial and sliding conditions along the tool-chip contact in machining differ significantly from that of conventional, lightly loaded, tribological contacts in two major aspects - the occurrence of plastic flow (in the chip) at the sliding interface and intimate nature of the contact where apparent and real contact areas are the same. In this study, we present an experimental method for direct measurement of the tool-chip contact stresses. This involves the use of sapphire as a cutting tool coupled with digital photoelasticity to obtain full-field principal stress difference (isochromatics) and principal stress directions (isoclinics). This enables direct full-field characterization of the tool-chip contact stresses, as well as stresses within the cutting tool, at a micronscale resolution not achieved previously. Our results show that the shear stress exhibits a maximum at a small distance from the tool tip, while the normal stress decreases monotonically with increasing distance from the tool tip. The maximum shear stress shows a good correlation with the shear flow stress of the material that is being machined. We also briefly discuss applications of the method to derive the stress distribution at the tool flank face and quantify frictional dissipation at both the contacts – tool-chip contact and flank-machined surface contact.

Keywords: cutting, digital photoelasticity, friction

1. INTRODUCTION

Interfacial condition at the tool-chip contact plays a major role in machining through its influence on the chip formation mode, specific cutting energy, temperature rise, and the tool wear [1–4]. It has been well-known that the traditional analysis of friction, where the friction force is assumed to vary in proportion to the normal force (Coulomb's law) does not accurately describe frictional conditions at the tool-chip contact [5]. This is because the interfacial and sliding conditions along the tool-chip contact in machining differ significantly from those of conventional, lightly

loaded, tribological contacts. For example, not only the chip material experiences plastic deformation parallel to the interface as sliding occurs, but also the chip underside that is in contact with the tool is a freshly generated surface that is pristine (free of surface oxide layer) [6, 7]. These factors result in a highly intimate sliding contact, where both the apparent and actual contact areas are almost identical [8].

Experimental techniques that have been used in the past to investigate tool-chip contact mechanics and stress distribution along the contact include instrumented split tools [9–12], moire technique [13], and photoelasticity [14–19]. The moire technique was found to have very limited stress sensitivity, while the split tool method is cumbersome and is also limited in terms of its ability to measure stresses close to the cutting edge. Photoelasticity, on the other hand, has proven to be a practical experimental technique for accurately characterizing tool-chip contact stress distribution. The early application of photoelasticity to machining involved the use of birefringent plastics pressed against specially designed models [14] and ready-made chips [20] to simulate the tool-chip contact. This method involved retracting the steel tool that was originally used to produce the chip and then pressing the ready-made chip with a photoelastic tool; this meant that the stress profiles obtained were not representative of the actual cutting process. For example, Ref. [15] shows that the fringe patterns observed in an epoxy tool while cutting soft lead are quite different from those observed in a tool pressed against a ready-made chip.

Subsequent photoelastic studies focused on characterizing the tool-chip contact stress distribution during the actual cutting process using birefringent plastics as cutting tool materials in conjunction with conventional photoelasticity to obtain data points along the tool-chip interface [15–17, 21]. However, the use of plastic tools meant that only soft metals like lead could be investigated. Despite this limitation, these studies, starting with Usui and Takeyama [15], yielded important information about the tool-chip contact stress distribution. These studies have suggested that while a large gradient in the normal stress exists along the contact, with the normal stress monotonically

^{*}Corresponding author: jobin@tamu.edu

decreasing from the tool tip to the chip separation point, the shear stress is uniformly distributed over a major portion of the contact length. Chandrasekaran and Kapoor's study [16] with different rake-angle tools reinforced these observations of nearly uniform shear stress along the contact, while Amini's study [17] suggested a different trend — that of monotonically increasing shear stress towards the tool tip. In this regard, it should be noted that all these studies relied on the conventional photoelasticity method, where the number of data points along the contact depends on the number of fringes that fall within the contact length. Consequently, the resolution of stress measurements along the contact is limited, which makes it challenging to resolve the stress data close to the cutting tip without ambiguity. This limitation led the previous researchers to either speculate stresses close to the tool tip or present data obtained by extrapolating the far-field stress profiles to the tool tip. The contrasting views regarding the interfacial stress distribution noted above are likely a consequence of this issue [22].

The next major advance came from Bagchi and Wright [19] who used sapphire as a cutting tool material in their photoe-lasticity study. Sapphire is chemically inert, has a high hardness comparable to commercial tool materials, and also exhibits stress-induced birefringence along its optic axis. This enabled stresses to be measured while cutting harder materials such as brass and steel at high speeds (up to ~ 1 m/s). Their observations with these materials largely supported earlier observations [15, 16, 21] and further indicated that under negative rake angles, the tool-chip contact shear stress is not uniform but exhibits a maximum near mid-way of the contact length before dropping to zero at the edge of the contact. Similar to earlier photoelasticity studies, the data resolution of Bagchi and Wright's measurements was again limited by the number of fringes along the contact length.

In this paper, we build on Bagchi and Wright's idea of using sapphire as a cutting tool and combine it with the digital photoelasticity method to obtain full-field stress distribution over the cutting tool at a high spatial (micron-scale) resolution not achieved previously. We present the basic principles of full-field photoelasticity and its application to measure stress distribution in steady-state continuous chip formation in single-phase 70-30 brass. It is shown that the use of digital photoelasticity offers fullfield data at enhanced resolution, allowing accurate measurement of stresses closest to the tool tip. Additionally, it provides a means to measure stress distribution at the flank-machined surface rubbing contact in isolation from the tool-chip contact. Normal and shear stress profiles along the tool rake face and flank face are clearly brought out using this method, and a simple method to quantify the individual contributions of tool-chip contact and flank-machined surface contact to the overall friction work is presented.

2. EXPERIMENTAL

Digital photoelasticity is a full-field experimental technique using light as a sensor, based on the property of temporary stress-induced birefringence. As the polarized light passes through a photoelastic material, the principal stress directions at a point act as the polarizing axes, and the two refracted rays travel at different velocities, causing a relative retardation. Two different types

of fringes can be observed in photoelasticity, namely, isoclinics and isochromatics. Isoclinics appear when the principal stress direction at a point coincides with the polarization direction of the plane-polarized light. Thus, the isoclinic fringe corresponds to the principal stress direction. The isochromatic fringes occur due to the retardation and are related to the principal stress difference. The isochromatic fringes appear as dark and bright fringes when the light source is monochromatic and colored when the light source is white light. The isoclinic fringe remains black for any light source used. The technique uses an experimental arrangement called polariscope (see Fig. 1), involving polarizers and quarter-wave plates. A plane polariscope arrangement (using the arrangement: light source / polarizer / photoelastic model / analyzer), gives both isoclinic and isochromatic fringes. Isoclinics can be removed using a circular polariscope arrangement (using the arrangement: light source / polarizer / quarter wave plate / photoelastic model / quarter wave plate / analyzer), giving only isochromatic fringes. Thus, photoelasticity provides fringe patterns corresponding to the principal stress difference and principal stress direction. However, to obtain full-field data, digital photoelasticity involving phase shifting techniques and image processing is required.

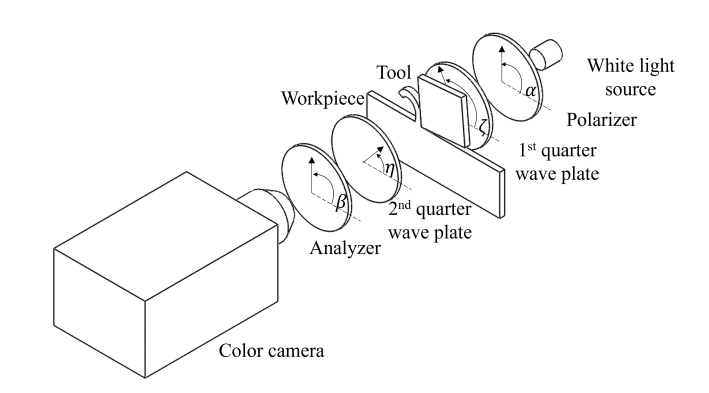


FIGURE 1: SCHEMATIC OF THE POLARISCOPE ARRANGEMENT CONSISTING OF A WHITE LIGHT SOURCE, POLARIZER, QUARTER WAVE PLATES, ANALYZER, CAMERA, AND SAPPHIRE CUTTING TOOL IN BETWEEN THE TWO QUARTER WAVE PLATES.

Ten-step phase shifting algorithm (PST) [23, 24] is one of the widely accepted phase shifting techniques developed for the estimation of full-field photoelastic data. Ten-step PST involves four images in the plane polariscope arrangement for the estimation of the isoclinic parameter and six images in the circular polariscope arrangement for the estimation of full field isochromatic parameter (see Table 1). The dedicated four images allow for accurate estimation of principal stress direction, eliminating quarter wave plate mismatch error. Further, the use of white light while capturing the plane polariscope images eliminates the error due to isoclinic-isochromatic interaction. The isoclinic parameter (principal stress direction) is obtained from the first four images using

$$\theta = \frac{1}{4} \tan^{-1} \left(\frac{I_4 - I_2}{I_3 - I_1} \right). \tag{1}$$

Similarly, the six images are used to estimate the isochromatic

TABLE 1: TEN-STEP METHOD: OPTICAL ARRANGEMENT AND RESPECTIVE INTENSITY EQUATIONS.

	α	ζ	η	β	Intensity Equation
Plane polariscope	$\frac{\pi}{2}$	-	-	0	$I_1 = I_b + I_a \sin^2(\frac{\delta}{2}) \sin^2 2\theta$
	$ \frac{\frac{\pi}{2}}{\frac{5\pi}{8}} \frac{\frac{3\pi}{4}}{\frac{7\pi}{8}} $	-	-	$\frac{\pi}{8}$	$I_2 = I_b + \frac{I_a}{2} \sin^2(\frac{\delta}{2})(1 - \sin 4\theta)$
	$\frac{3\pi}{4}$	-	-	$\frac{\frac{\pi}{4}}{\frac{3\pi}{8}}$	$I_3 = I_b + I_a \sin^2(\frac{\delta}{2}) \cos^2 2\theta$
	$\frac{7\pi}{8}$	-	-	$\frac{3\pi}{8}$	$I_4 = I_b + \frac{I_a}{2}\sin^2(\frac{\delta}{2})(1 + \sin 4\theta)$
Circular polariscope	$\frac{\pi}{2}$	$\frac{3\pi}{4}$	$\frac{\pi}{4}$	$\frac{\pi}{2}$	$I_5 = I_b + \frac{I_a}{2}(1 + \cos \delta)$
	$\frac{\pi}{2}$	$ \begin{array}{c} 4 \\ 3\pi \\ 4 \\ 3\pi \\ 4 \\ 3\pi \\ 4 \\ \pi \\ 4 \\ \pi \\ 4 \end{array} $	$\frac{\frac{\pi}{4}}{\frac{\pi}{4}}$	0	$I_6 = I_b + \frac{I_a}{2}(1 - \cos \delta)$
	$\frac{\pi}{2}$	$\frac{3\pi}{4}$	0	0	$I_7 = I_b + \frac{I_a}{2}(1 - \sin 2\theta \sin \delta)$
	$\frac{\pi}{2}$	$\frac{3\pi}{4}$	$\frac{\pi}{4}$	$\frac{\pi}{4}$	$I_8 = I_b + \frac{I_a}{2}(1 + \cos 2\theta \sin \delta)$
	$\frac{\pi}{2}$	$\frac{\pi}{4}$	0	0	$I_9 = I_b + \frac{I_a}{2}(1 + \sin 2\theta \sin \delta)$
	$\frac{\pi}{2}$	$\frac{\pi}{4}$	$\frac{3\pi}{4}$	$\frac{\pi}{4}$	$I_{10} = I_b + \frac{I_a}{2}(1 - \cos 2\theta \sin \delta)$

parameter using

$$\delta = \tan^{-1} \left(\frac{(I_9 - I_7)\sin 2\theta + (I_8 - I_{10})\cos 2\theta}{(I_5 - I_6)} \right), \tag{2}$$

where $\delta = 2\pi N$, with N being the fringe order. The results obtained from Eq. 1 may contain inconsistent regions with the direction of the second principal stress and Eq. 2 generates bands of fractional fringe orders. The generation of continuous isoclinic and isochromatic data requires phase unwrapping. To this end, an adaptive quality guided phase unwrapping (AQGPU) algorithm [25] is used in this work. The principal stress difference is obtained from the fringe order using the stress optics law:

$$\sigma_1 - \sigma_2 = \frac{Nf_{\sigma}}{h},\tag{3}$$

where f_{σ} is the material stress fringe value and h is the thickness. Using the full-field principal stress difference and the principal stress direction, the difference in normal stress components and the shear stress are obtained as follows:

$$\sigma_{xx} - \sigma_{yy} = (\sigma_1 - \sigma_2)\cos 2\theta,$$

$$\tau_{xy} = \frac{\sigma_1 - \sigma_2}{2}\sin 2\theta.$$
(4)

Next, the individual components of the stress tensor are estimated over the entire domain using the shear difference technique [26]. This technique uses the finite difference approximation of the equilibrium equation and requires a point in the domain with complete stress information. If we consider a point on the free boundary with an outward normal along the y-axis ($\sigma_{yy}^i = 0$, $\tau_{xy}^i = 0$), where all the individual stress components are known (from Eq. 4), then the individual stress components for all points along the y-axis can be obtained using the shear difference equation:

$$\sigma_{yy}^{j} = \sigma_{yy}^{i} - \sum_{i}^{j} \frac{\Delta \tau_{xy}}{\Delta x} \Delta y. \tag{5}$$

All these points act as seed points in the marching algorithm for stress separation along the x-axis. Since the calculation of shear slope in the shear difference equation often leads to error accumulation, an improved version of the shear difference technique [27]

$$\sigma_{yy}^{j} = \sigma_{yy}^{i} - \sum_{i}^{j} \frac{\Delta(\sigma_{1} - \sigma_{2})}{\Delta x} \frac{\sin 2\theta}{2} \Delta y - \sum_{i}^{j} (\sigma_{1} - \sigma_{2}) \cos 2\theta \frac{\Delta\theta}{\Delta x} \Delta y$$
(6)

 $\begin{array}{c} 0 & I_1 = I_b + I_a \sin^2(\frac{c}{2}) \sin^2 2\theta \\ \frac{\pi}{8} & I_2 = I_b + \frac{I_b}{2} \sin^2(\frac{c}{2}) (1 - \sin 4\theta) \\ \frac{\pi}{4} & I_3 = I_b + I_a \sin^2(\frac{c}{2}) \cos^2 2\theta \\ \frac{\pi}{3} & I_4 = I_b + \frac{I_b}{2} \sin^2(\frac{c}{2}) (1 + \sin 4\theta) \\ \frac{\pi}{2} & I_5 = I_b + \frac{I_a}{2} (1 - \cos \delta) \\ 0 & I_6 = I_b + \frac{I_a}{2} (1 - \cos \delta) \\ 0 & I_7 = I_b + \frac{I_b}{2} (1 - \cos 2\theta \sin \delta) \\ \frac{\pi}{4} & I_8 = I_b + \frac{I_a}{2} (1 - \cos 2\theta \sin \delta) \\ 0 & I_9 = I_b + \frac{I_b}{2} (1 - \cos 2\theta \sin \delta) \\ \frac{\pi}{4} & I_{10} = I_b + \frac{I_b}{2} (1 - \cos 2\theta \sin \delta) \\ \frac{\pi}{4} & I_{10} = I_b + \frac{I_b}{2} (1 - \cos 2\theta \sin \delta) \\ \frac{\pi}{4} & I_{10} = I_b + \frac{I_b}{2} (1 - \cos 2\theta \sin \delta) \\ \frac{\pi}{4} & I_{10} = I_b + \frac{I_b}{2} (1 - \cos 2\theta \sin \delta) \\ \frac{\pi}{4} & I_{10} = I_b + \frac{I_b}{2} (1 - \cos 2\theta \sin \delta) \\ \frac{\pi}{4} & I_{10} = I_b + \frac{I_b}{2} (1 - \cos 2\theta \sin \delta) \\ \frac{\pi}{4} & I_{10} = I_b + \frac{I_b}{2} (1 - \cos 2\theta \sin \delta) \\ \frac{\pi}{4} & I_{10} = I_b + \frac{I_b}{2} (1 - \cos 2\theta \sin \delta) \\ \frac{\pi}{4} & I_{10} = I_b + \frac{I_b}{2} (1 - \cos 2\theta \sin \delta) \\ \frac{\pi}{4} & I_{10} = I_b + \frac{I_b}{2} (1 - \cos 2\theta \sin \delta) \\ \frac{\pi}{4} & I_{10} = I_b + \frac{I_b}{2} (1 - \cos 2\theta \sin \delta) \\ \frac{\pi}{4} & I_{10} = I_b + \frac{I_b}{2} (1 - \cos 2\theta \sin \delta) \\ \frac{\pi}{4} & I_{10} = I_b + \frac{I_b}{2} (1 - \cos 2\theta \sin \delta) \\ \frac{\pi}{4} & I_{10} = I_b + \frac{I_b}{2} (1 - \cos 2\theta \sin \delta) \\ \frac{\pi}{4} & I_{10} = I_b + \frac{I_b}{2} (1 - \cos 2\theta \sin \delta) \\ \frac{\pi}{4} & I_{10} = I_b + \frac{I_b}{2} (1 - \cos 2\theta \sin \delta) \\ \frac{\pi}{4} & I_{10} = I_b + \frac{I_b}{2} (1 - \cos 2\theta \sin \delta) \\ \frac{\pi}{4} & I_{10} = I_b + \frac{I_b}{2} (1 - \cos 2\theta \sin \delta) \\ \frac{\pi}{4} & I_{10} = I_b + \frac{I_b}{2} (1 - \cos 2\theta \sin \delta) \\ \frac{\pi}{4} & I_{10} = I_b + \frac{I_b}{2} (1 - \cos 2\theta \sin \delta) \\ \frac{\pi}{4} & I_{10} = I_b + \frac{I_b}{2} (1 - \cos 2\theta \sin \delta) \\ \frac{\pi}{4} & I_{10} = I_b + \frac{I_b}{2} (1 - \cos 2\theta \sin \delta) \\ \frac{\pi}{4} & I_{10} = I_b + \frac{I_b}{2} (1 - \cos 2\theta \sin \delta) \\ \frac{\pi}{4} & I_{10} = I_b + \frac{I_b}{2} (1 - \cos 2\theta \sin \delta) \\ \frac{\pi}{4} & I_{10} = I_b + \frac{I_b}{2} (1 - \cos 2\theta \sin \delta) \\ \frac{\pi}{4} & I_{10} = I_b + \frac{I_b}{2} (1 - \cos 2\theta \sin \delta) \\ \frac{\pi}{4} & I_{10} = I_b + \frac{I_b}{2} (1 - \cos 2\theta \sin \delta) \\ \frac{\pi}{4} & I_{10} = I_b + \frac{I_b}{2} (1 - \cos 2\theta \sin \delta) \\ \frac{\pi}{4} & I_{10} = I_b + \frac{I_b}{2} (1 - \cos 2\theta \sin \delta) \\ \frac{\pi}{4} & I_{10} = I_b + \frac{I_b}{2} (1 - \cos 2\theta \sin \delta) \\ \frac{\pi}{4} & I_{10} = I_b + \frac{I_b}{2} (1 - \cos 2\theta \sin \delta) \\ \frac{\pi}$

Digital photoelasticity measurements have enabled quantitative analysis of tool-chip contact stresses (and stresses within the cutting tool) at high spatial resolution and also allowed delin-

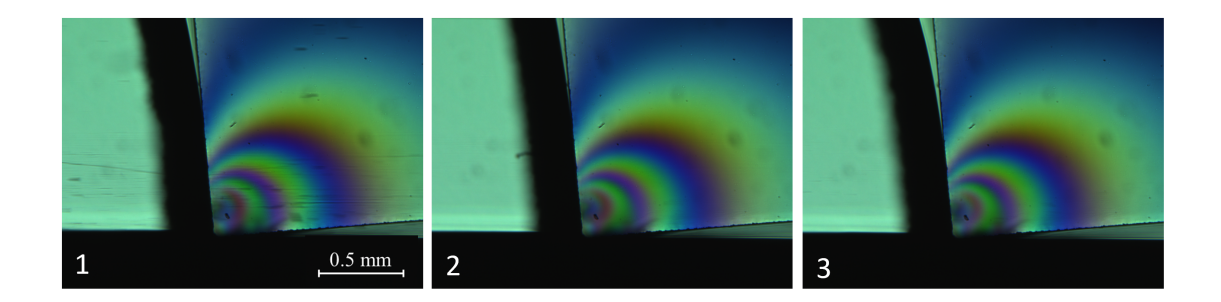


FIGURE 2: BRIGHT-FIELD CIRCULAR POLARISCOPE IMAGES OBTAINED AT DIFFERENT INSTANCES OF THE CUTTING PROCESS. DISTRIBUTION OF FRINGES IS IDENTICAL AT DIFFERENT TIMES, INDICATING STEADY-STATE NATURE OF THE CUTTING/CHIP FORMATION PROCESS. WORKPIECE: 70-30 BRASS, $\alpha = -5^{\circ}$, $t_0 = 45 \mu \text{M}$, $V_0 = 2 \text{ MM/S}$.

eation of tool-chip contact friction from friction at the tool flank face.

3.1 Stress distribution in machining

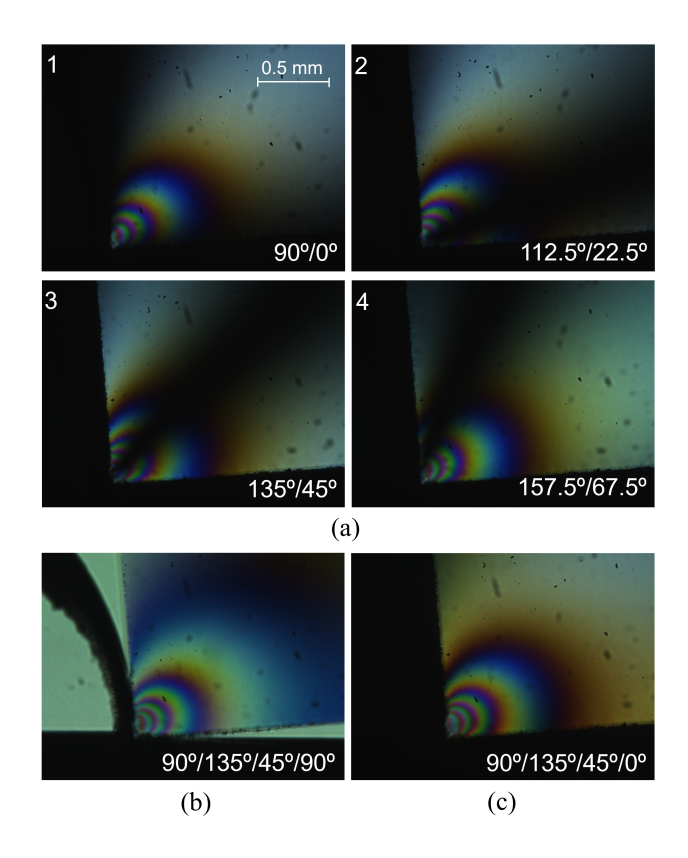


FIGURE 3: (A) PLANE POLARISCOPE IMAGES OBTAINED UNDER DIFFERENT POLARIZER/ANALYZER ARRANGEMENTS. (B) AND (C) ARE RESPECTIVELY THE BRIGHT-FIELD AND DARKFIELD CIRCULAR POLARISCOPE IMAGES. EXPERIMENTAL CONDITIONS: $\alpha=-5^\circ,\,t_0=45~\mu\mathrm{M},\,V_0=0.5~\mathrm{MM/S}.$

Figure 2 shows bright-field circular polariscope images captured at different time instances during cutting of 70-30 brass with a sapphire tool having a -5° rake angle; the relief angle on the tool at the flank face is 5° . As noted earlier, the experimental

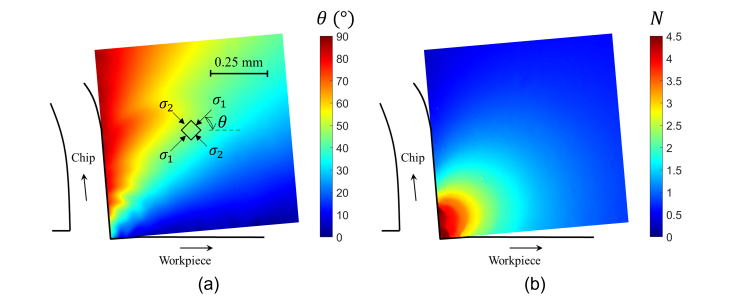


FIGURE 4: FULL-FIELD MAPS SHOWING THE (A) PRINCIPAL STRESS DIRECTION (θ) AND (B) FRINGE ORDER (N) OVER THE CUTTING TOOL. θ REPRESENTS THE ORIENTATION OF MAJOR PRINCIPAL STRESS (σ_1) MEASURED COUNTER-CLOCKWISE FROM THE HORIZONTAL (V_0) DIRECTION.

configuration is such that the workpiece moves past the sapphire tool with a constant velocity, producing a continuous chip. As can be seen from the images, there is little change in the fringe contours during cutting, which reflects the steady-state nature of the cutting process. In this regard, it should be noted that the phase shifting technique discussed earlier for obtaining full-field stress data requires ten sets of images, ideally captured at the same time instance. However, the steady-state nature of continuous chip formation bypasses this need as images captured at different time instances can be used in the phase shifting technique. This is the approach adopted in this study.

Figure 3 (a) shows four images captured in the plane polariscope arrangement (see Table 1) at different time instances of a similar cutting experiment. As can be seen, the isochromatics (colored fringes) remain identical, while the isoclinics (black fringe) rotate as the polarizer and analyzer are rotated together. The images correspond to 0° , 22.5° , 45° , and 67.5° isoclinics. This set of four images is used in the AQGPU algorithm to obtain full-field data of the principal stress direction (θ). Similarly, Figs. 3 (b) and (c) show the corresponding bright-field and darkfield images, which are the first two configurations in the circular polariscope arrangement in Table 1. Six images such obtained in the circular polariscope arrangement are used to obtain full-field data of the fringe order (N).

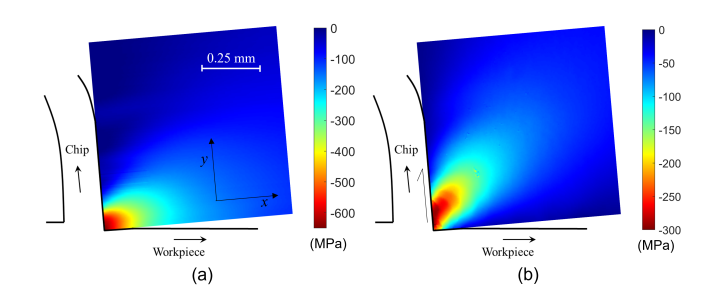


FIGURE 5: FULL-FIELD MAPS SHOWING (A) NORMAL (σ_{xx}) AND (B) SHEAR (τ_{xy}) STRESSES IN THE CUTTING TOOL, AS OBTAINED USING THE SHEAR DIFFERENCE TECHNIQUE. σ_{xx} IS THE STRESS COMPONENT ACTING PERPENDICULAR TO THE TOOL RAKE FACE (NEGATIVE SIGN MEANS THAT THE STRESS IS COMPRESSIVE), WHILE τ_{xy} IS THE SHEAR COMPONENT ALONG THE RAKE FACE (NEGATIVE SIGN REPRESENTS CLOCK-WISE SHEAR).

Figure 4 shows the full-field maps of principal stress direction and fringe order obtained using the phase shifting algorithm and the AQGPU method. The principal stress direction (θ) is defined as the angle the major principal stress (σ_1) makes with respect to the horizontal V_0 direction. Full-field maps of σ_{xx} and τ_{xy} components obtained from θ and N using the shear difference technique are shown in Fig. 5. Here, x and y represent directions that are normal and parallel to the tool rake face, respectively (see Fig. 5(a)). Therefore, σ_{xx} is the normal stress acting perpendicular to the rake face, while τ_{xy} is the shear stress along the rake face. In the shear difference technique, a point on the flank face away from the tool tip was used as a seed point for the shear difference technique. In our convention, negative values of the normal stress indicate the compressive stress state while negative shear stress values indicate shear in the clockwise direction. As can be seen from the normal stress distribution in Fig. 5(a), the stress state is compressive near the tool-chip contact region, with the normal stress showing a maximum at the tool tip. The shear stress distribution in Fig. 5(b) on the other hand shows an interesting behavior where the maximum is located not at the tool tip but about a 50 μ m distance from the cutting tool tip; we will return to this topic in Sec. 3.2.

In order to validate the stress measurements, the individual components of the stress tensor were integrated over both the rake and flank faces to arrive at an estimate of the total cutting and thrust forces acting on the tool. This resulted in the following estimates: $F_C = 249 \text{ N}$ and $F_T = 220$, which are close to the steady-state F_C (260 N) and F_T (230 N) values measured using the dynamometer for that particular experiment.

3.2 Rake face and flank face stress profiles

In order to understand local stress variations along the toolchip contact and flank-machined surface contact, stress profiles along the rake face and flank face are presented in Figs. 6(a) and (b), respectively. The figures show both the normal and shear stresses along these two faces plotted as a function of distance from the cutting tool tip. As can be seen from Fig. 6(a), the

normal stress (σ_R) at the too-chip contact is maximum at the tool tip and decreases monotonically with increasing distance from the tip, eventually reaching zero at the end of the contact length ($\sim 400 \ \mu m$). In contrast, the shear stress (τ_R) profile is non-monotonic. The maximum shear stress does not coincide with the tool tip but is observed at about 50 μ m distance from the tool tip; this is followed by a continuous decrease in the shear stress towards the end of the contact. Comparison of the peak shear stress (~ 300 MPa) at the tool-chip contact with the material's shear flow stress (322 MPa) shows that they are indeed close, suggesting that the shear stress at this contact is limited by plastic yielding of the chip; shear flow stress of the chip, τ_Y , was estimated using the classical shear plane model [31] from the measured F_C and F_T data and the shear plane angle (ϕ) as follows: $\tau_Y = \frac{(F_C \cos \phi - F_T \sin \phi) \sin \phi}{bt_0}$, where b is the chip width and t_0 is the depth of cut. This also provides a reason to believe that the tool-chip contact region beyond the peak shear stress is elastically loaded, while the region near the tool tip is in a state of plastic yielding. In contrast to the rake face, both the normal (σ_F) and shear (τ_F) stresses at the flank face decreases monotonically with increasing distance from the cutting edge, see Fig. 6(b). The length of the flank-machined surface contact is about 100 μ m, and the fact that the peak τ_F at the tool tip is considerably lower than the material's shear flow stress suggests that this contact is nominally elastic.

An interesting application of our photoelasticity measurements is that it allows for separate calculations of the friction work associated with tool-chip and flank-machined surface contacts. For example, friction work (per unit time) at the tool-chip contact can be estimated from $b \int T_R \cdot V_C$ evaluated over the contact length, with T_R being the traction vector and V_C the sliding velocity of the chip with respect to the rake face. Taking V_C to be constant along the rake face, at $V_0 t_0 / t_c$ (t_c is the average chip thickness), the tool-chip contact friction work was estimated to be 22% of the total work. Friction work at the flank-machined surface contact can be similarly obtained from $b \int T_F \cdot V_0$; this shows flank face friction is comparable to the rake face friction and contributes to 14% of the total work under the cutting conditions investigated here.

4. DISCUSSION

The results have shown that the use of sapphire tools coupled with digital photoelasticity is an effective experimental technique to quantify tool-chip contact stress distribution in machining. While the high hardness of sapphire allows machining of most metals (including steels), high-resolution full-field stress data that can be obtained using the digital photoelasticity method allows detailed characterization of steep stress gradients near the cutting edge. As noted earlier, the resolution of stresses in the immediate vicinity of the tool tip has been traditionally difficult and a key limitation in earlier studies of contact stresses in machining.

Contradicting viewpoints exist in the literature regarding stress distribution at the tool-chip contact [22, 32]. While this could be in part due to differences in the cutting conditions and tool/workpiece materials used in different studies, we believe that measurement resolution is at least as big a factor. Conventional photoelasticity provides a limited number of data points along the

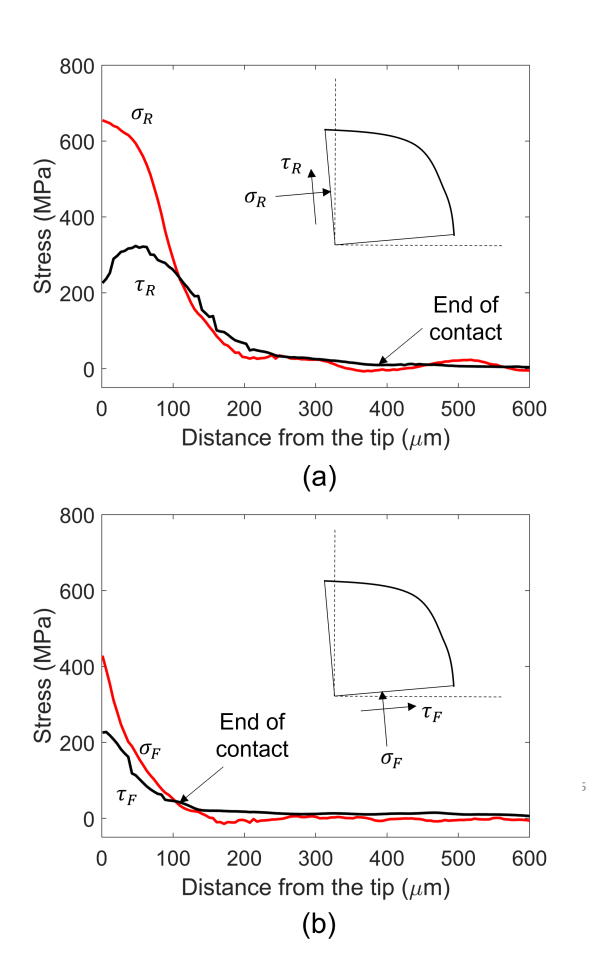


FIGURE 6: NORMAL (RED) AND SHEAR (BLACK) STRESS PROFILES ALONG THE (A) RAKE FACE AND (B) FLANK FACE OF THE CUTTING TOOL. END OF THE CONTACT WHERE STRESSES DROP TO ZERO IS SHOWN USING AN ARROW FOR BOTH THE CASES.

tool-chip interface, and as a result, stresses close to the cutting edge are often speculated or obtained via extrapolation of data points located away from the tool tip. This study shows how the use of digital photoelasticity can address this issue and provide full-field stress data at improved resolution when compared to existing stress measurement techniques. Improved resolution offers several benefits, including the ability to resolve the variation of stresses along the interface accurately; characterization of stress distribution at the tool flank face; and the capability to study tool-chip interfacial conditions under realistic depths of cut. In the latter regard, due to resolution limitations of conventional photoelasticity, several studies in the literature employed relatively large cutting depths [15, 16].

An interesting observation from the study is the occurrence of the peak in the shear stress at about mid-way of the tool-chip contact length, which is in contrast with the constant shear stress distribution that is often assumed in the modeling of machining. While the possibility of such a peak has been suggested by earlier photoelasticity studies by Chandrasekaran and Kapoor [16] and later by Bagchi and Wright [19], our high-resolution measurements bring out this feature without ambiguity and further show

that the shear stress at the tool tip takes a small finite value, but is not zero. The origin of this peak and why the region immediately adjacent to the tool tip exhibits low shear stress values remain to be understood, but it is likely that interfacial stress profiles are tightly linked to the local sliding conditions at the contact. For example, direct observations of sliding at the tool-chip contact using transparent cutting tools [6, 32-34] have shown that the tool-chip contact can be divided into distinct regions: sticking region near the chip separation point (edge of the contact), sliding region, a region of retardation, and a stagnation region close to the cutting edge. The dip in shear stress close to the tool tip suggests a possible correlation with the stagnation region. Measurements of tool-chip interfacial stresses in tandem with direct observations of the sliding process, and how they vary with the cutting conditions would certainly be valuable. Our study has focused on steady-state chip formation under low cutting speeds. It would be also of interest to extend the approach outlined in this paper to higher cutting speeds and to study time-varying stresses associated with non-steady chip formation modes such as segmented and shear-localized chips [35, 36].

5. CONCLUSION

This study has described the application of digital photoelasticity method coupled with sapphire as a cutting tool material to determine tool-chip contact stresses and full-field stress distribution within the cutting tool at high spatial resolution. Ductile single-phase brass was used as a model material to effect steady-state continuous chip formation. The study reveals several interesting features of the tool-chip contact, including nonmonotonic shear stress variation along the contact and a possible elastic-plastic transition near the trailing edge of the contact. In particular, it was shown that the shear stress exhibits a maximum at a small distance from the tool tip, while the normal stress decreases monotonically with increasing distance from the tool tip. The high resolution of the method also enables characterization of steep stress gradients at the tool flank face. Application of the method to estimate individual friction contributions associated with the tool-chip sliding contact and rubbing at the flank face to the overall cutting energy is presented.

ACKNOWLEDGMENTS

The work was supported by the US National Science Foundation through grant no. CMMI-2102030; and the TAMUS National Laboratories Office (NLO) Los Alamos National Laboratory (LANL) Collaborative Research Program through award no. CF5789.

REFERENCES

- [1] Ernst, H. and Merchant, M. E. *Chip formation, friction and finish*. American Society for Metals (1941): pp. 299–378.
- [2] Trent, E. M. Metal Cutting. Butterworths, London (1977).
- [3] Zorev, N. N. *Metal Cutting Mechanics*. Pergamon Press, Oxford, England (1966).
- [4] Feng, G. and Sagapuram, D. "A strong basis for friction as the origin of size effect in cutting of metals." *International Journal of Machine Tools and Manufacture* Vol. 168 (2021): p. 103741.

- [5] Finnie, I. and Shaw, M. C. "The friction process in metal cutting." *Transactions of the American Society of Mechanical Engineers* Vol. 78 No. 8 (1956): pp. 1649–1653.
- [6] Doyle, E. D., Horne, J. G. and Tabor, D. "Frictional interactions between chip and rake face in continuous chip formation." *Proceedings of the Royal Society of London. A. Mathematical and Physical Sciences* Vol. 366 No. 1725 (1979): pp. 173–183.
- [7] Wright, P. K., Horne, J. G. and Tabor, D. "Boundary conditions at the chip-tool interface in machining: Comparisons between seizure and sliding friction." *Wear* Vol. 54 No. 2 (1979): pp. 371–390.
- [8] Nakayama, K. "Studies on the mechanism of metal cutting." *Bulletin of the Faculty of Engineering, Yokohama National University* Vol. 7 (1959): pp. 1–26.
- [9] Kato, S., Yamaguchi, K. and Yamada, M. "Stress distribution at the interface between tool and chip in machining." *Journal of Engineering for Industry* Vol. 94 (1972): pp. 683–689.
- [10] Barrow, G., Graham, W., Kurimoto, T. and Leong, Y. F. "Determination of rake face stress distribution in orthogonal machining." *International Journal of Machine Tool Design* and Research Vol. 22 No. 1 (1982): pp. 75–85.
- [11] Childs, T. H. C., Mahdi, M. I. and Barrow, G. "On the stress distribution between the chip and tool during metal turning." *CIRP Annals* Vol. 38 No. 1 (1989): pp. 55–58.
- [12] Buryta, D., Sowerby, R. and Yellowley, I. "Stress distributions on the rake face during orthogonal machining." *International Journal of Machine Tools and Manufacture* Vol. 34 No. 5 (1994): pp. 721–739.
- [13] Chandrasekaran, H., Nagarajan, R. and Padmanabha, K. N. "Application of moiré technique in the stress analysis of cutting tools." *Strain* Vol. 14 No. 2 (1978): pp. 64–71.
- [14] Okoshi, M. and Fukui, S. "Studies of cutting action by means of photoelasticity." *Journal of the Society of Precision Mechanics of Japan* Vol. 1 (1934): p. 598.
- [15] Usui, E. and Takeyama, H. "A photoelastic analysis of machining stresses." *Journal of Engineering for Industry* Vol. 84 (1960): pp. 303–307.
- [16] Chandrasekaran, H. and Kapoor, D. V. "Photoelastic analysis of tool-chip interface stresses." *Journal of Engineering for Industry* Vol. 87 (1965): pp. 495–502.
- [17] Amini, E. "Photoelastic analysis of stresses and forces in steady cutting." *Journal of Strain Analysis* Vol. 3 No. 3 (1968): pp. 206–213.
- [18] Ramalingam, S. "A photoelastic study of stress distribution during orthogonal cutting Part 2: Photoplasticity observations." *Journal of Engineering for Industry* Vol. 93 (1971): pp. 538–544.
- [19] Bagchi, A. and Wright, P. K. "Stress analysis in machining with the use of sapphire tools." *Proceedings of the Royal Society of London. A. Mathematical and Physical Sciences* Vol. 409 No. 1836 (1987): pp. 99–113.
- [20] Coker, E. G. "Cutting tools research committee. Report on the action of cutting tools." *Proceedings of the Institution of Mechanical Engineers* Vol. 108 No. 1 (1925): pp. 357–382.

- [21] Kattwinkel, W. "Experimentation of cutting action by means of photoelasticity." *Industrie Anzeiger* Vol. 36 (1957): pp. 525–532.
- [22] Arsecularatne, J. A. "On tool-chip interface stress distributions, ploughing force and size effect in machining." *International Journal of Machine Tools and Manufacture* Vol. 37 No. 7 (1997): pp. 885–899.
- [23] Ramji, M. and Ramesh, K. "Whole field evaluation of stress components in digital photoelasticity—Issues, implementation and application." *Optics and Lasers in Engineering* Vol. 46 No. 3 (2008): pp. 257–271.
- [24] Jobin, T. M., Khaderi, Syed Nizamuddin and Ramji, M. "Experimental evaluation of the strain intensity factor at the inclusion tip using digital photoelasticity." *Optics and Lasers in Engineering* Vol. 126 (2020): p. 105855.
- [25] Ramji, M. and Ramesh, K. "Adaptive quality guided phase unwrapping algorithm for whole-field digital photoelastic parameter estimation of complex models." *Strain* Vol. 46 No. 2 (2010): pp. 184–194.
- [26] Frocht, M. M. Photoelasticity. John Wiley and Sons, Inc., New York (1941).
- [27] Vadovič, F. "Contribution to the analysis of errors in photoelasticity: Application of theory of errors to some numerical methods used in photoelasticity to separate the principal stresses yields greater accuracy." *Experimental Mechanics* Vol. 5 (1965): pp. 413–416.
- [28] Timoshenko, S. and N., Goodier J. *Theory of Elasticity*. McGraw-Hill Book Company, New York (1951).
- [29] Yadav, S., Feng, G. and Sagapuram, D. "Dynamics of shear band instabilities in cutting of metals." *CIRP Annals* Vol. 68 No. 1 (2019): pp. 45–48.
- [30] Yadav, S. and Sagapuram, D. "In situ analysis of shear bands and boundary layer formation in metals." *Proceedings of the Royal Society A* Vol. 476 No. 2234 (2020): p. 20190519.
- [31] Shaw, M. C. Metal Cutting Principles. MIT Press, Cambridge, MA (1954).
- [32] Madhavan, V., Chandrasekar, S. and Farris, T. N. "Direct observations of the chip-tool interface in the low speed cutting of pure metals." *Journal of Tribology* Vol. 124 No. 3 (2002): pp. 617–626.
- [33] Horne, J. G. "The chip-tool interface in metal cutting." Ph.D. Thesis, University of Cambridge. 1978.
- [34] Ackroyd, B., Chandrasekar, S. and Compton, W. D. "A model for the contact conditions at the chip-tool interface in machining." *Journal of Tribology* Vol. 125 No. 3 (2003): pp. 649–660.
- [35] Sagapuram, D., Viswanathan, K., Mahato, A., Sundaram, N. K., M'Saoubi, R., Trumble, K. P. and Chandrasekar, S. "Geometric flow control of shear bands by suppression of viscous sliding." *Proceedings of the Royal Society A: Mathematical, Physical and Engineering Sciences* Vol. 472 No. 2192 (2016): p. 20160167.
- [36] Sagapuram, D., Udupa, A., Viswanathan, K., Mann, J. B., M'Saoubi, R., Sugihara, T. and Chandrasekar, S. "On the cutting of metals: A mechanics viewpoint." *Journal of Manufacturing Science and Engineering* Vol. 142 No. 11 (2020): p. 110808.